Analysis of wall temperature and heat flux distributions in a swirled combustor powered by a methane-air and a CO_2-diluted oxyflame

Arthur Degenève[a,b,*], Paul Jourdaine[b], Clément Mirat[a], Jean Caudal[b], Ronan Vicquelin[a], Thierry Schuller[a,c]

[a] Laboratoire EM2C, CNRS, CentraleSupélec, Université Paris-Saclay, 8-10 rue Joliot Curie 91192 Gif Sur Yvette Cedex, France
[b] Air Liquide, Centre de Recherche Paris-Saclay, 1, chemin de la Porte des Loges, Les Loges en Josas BP 126, 78354 Jouy-en-Josas Cedex, France
[c] Institut de Mécanique des Fluides de Toulouse, IMFT, Université de Toulouse, CNRS, Toulouse, France

ABSTRACT

The behavior of technically premixed CO_2-diluted methane oxyflames is compared to operation with methane-air flames in a labscale combustor equipped with an axial-plus-tangential swirler. It has been shown in a former study that the stabilization regimes and topologies of CO_2-diluted oxy-flames can be deduced from methane-air flames despite large changes of the oxidizer and fuel flowrates. This work proceeds and focuses on differences in distributions of wall temperature and wall heat fluxes for a methane-air and a CO_2-diluted methane oxyflame sharing the same thermal power, equivalence ratio, adiabatic flame temperature and swirl number. Laser-Induced Phosphorescence measurements are used to determine the temperature distributions along the combustor metallic back plane wall and along the internal and external surfaces of the quartz windows. These data are used to determine the local heat flux through the combustor windows. It is found that both the air and CO_2-diluted oxy-flames feature approximately the same temperature distributions and total thermal loads along the combustion chamber walls. As high concentrations of carbon dioxide are known to significantly enhance radiative heat transfer, an analysis is carried out so as to account for the mechanisms that provide this similarity in the wall temperatures and heat fluxes between the two flames. The low order model allows for determining the origin of the heat flux and shows how convective heat transfer is supplemented by radiative heat transfer when switching from air to CO_2-diluted oxy-combustion with a global thermal load that remains roughly unaltered for the studied combustion chamber.

1. Introduction

Revamping existing air powered combustors to oxycombustion operation with a limited number of modifications and without impairing performances and emissions raises many technical [1–4] and scientific issues [5–7].

In a recent work, Jourdaine et al. [8] investigated the stabilization of N_2- and CO_2-diluted premixed swirling flames over a wide range of combustion parameters. For a given thermal power, they found that the two main parameters controlling the flame topology and lift-off height above the swirling injector when switching from N_2 to CO_2 dilution were the adiabatic flame temperature T_{ad} and the ratio of the bulk flow velocity at the burner outlet to the laminar burning velocity U_b/S_L. A detailed analysis of the flow and flame structure was then carried out for a N_2-diluted ($X_{N_2} = 0.79$) and CO_2-diluted ($X_{CO_2} = 0.68$) flame featuring the same thermal power $\mathscr{P} = 13$ kW, equivalence ratio $\phi = 0.95$ and adiabatic flame temperature $T_{ad} = 2200$ K. Particle image velocimetry measurements revealed that the structure of the flowfield at the injector outlet was homothetic despite the large drop of the bulk flow velocity $U_b = 9.7$ m. s^{-1} for the CO_2-diluted flame compared to operation with air at $U_b = 14.3$ m. s^{-1}. It was also found that the burned gas temperature and the temperature at three distinct locations in the metallic components of the combustor were roughly the same between the N_2- and CO_2-diluted cases despite the large changes of the diluent thermal and radiative properties and flow velocities along the combustor walls.

Managing the thermal load on the injector nozzle and combustion chamber walls is a critical issue when operating the combustor with a modified combustible mixture. Heat losses to the walls are well known to greatly alter the flame topology [9–11]. Another difficulty is to account for the radiative properties of CO_2 that are likely to bring a major difference when switching from N_2- to CO_2-dilution operation.

Numerical simulations of channel flows filled with inert gases have shown that thermal radiation from participating gaseous species can strongly modify the turbulent temperature field within the flow [12–14] in addition to introducing a supplemental wall radiative flux. Coupling effects therefore alter both the distribution of temperature and the balance between radiative and convective contributions to the total wall heat flux. Thermal radiation modifies the temperature profile in the boundary layers [13] leading to a different wall temperature gradient and a different wall convective heat flux. On the one-hand, gas–gas interactions homogenize the core temperature field [13,15] and lead to increased wall temperature gradients and wall convective heat fluxes. On the other hand, gas-wall radiative interactions lead to a reduced wall convective heat flux. In a recent study, Koren et al. [15] coupled a Monte Carlo radiative transfer solver accounting for H_2O and CO_2 detailed radiative properties with a large eddy simulation study of conjugate heat transfer. The authors compared their numerical results with measurements gathered on a lab-scale swirled premixed combustor powered by a lean CH_4/H_2 and air mixture. They found that thermal radiation modifies both contributions of the total wall heat flux in a sizable manner despite the relatively moderate fractions of water vapor and carbon dioxide in the burned gases of the studied air powered system.

This has motivated the present study, where two flames sharing the same topology and same power have been selected in a configuration where the major abundant species N_2 is replaced by CO_2 [8]. The OH* chemiluminescence signals from the N_2-diluted flame, designated as Flame A in the following, and the CO_2-diluted flame, designated as Flame B are represented in Fig. 1. These flames share the same power ($\mathscr{P}$ = 13 kW), equivalence ratio (Φ = 0.95), adiabatic flame temperature (T_{ad} = 2200 K) and swirl number (S_0 = 0.75) with about the same ratio U_b/S_L. Dilution is characterized in this study by the molar fraction of CO_2 or N_2 in the oxidizer stream. Flame A is powered with air $X_{N_2} = 0.79$. Nitrogen is replaced by carbon dioxide in Flame B with a CO_2 molar fraction set to $X_{CO_2} = 0.68$ to reach the same adiabatic flame temperature. The main objectives of this article are to compare the wall temperature distributions and elucidate the redistribution of wall heat fluxes between these two cases.

The article is organized as follows. The test-rig and the optical diagnostics are presented in Section 2. Temperature measurements along the walls of the combustion chamber are then presented for Flame A and Flame B in Section 3.1. A focus is made on the temperatures recorded at the internal and external surface of the combustion chamber quartz windows. The conductive heat flux through the quartz window is derived from these latter temperature profiles. An analysis of the contributions to the total wall heat flux and the distribution of this heat flux at the combustion chamber sidewalls is finally carried out to infer the distributions of surface temperatures observed for flames A and B. This allows the determination of the predominant heat transfer regime in the different regions of the combustion chamber. The main conclusions are synthesized in Section 4.

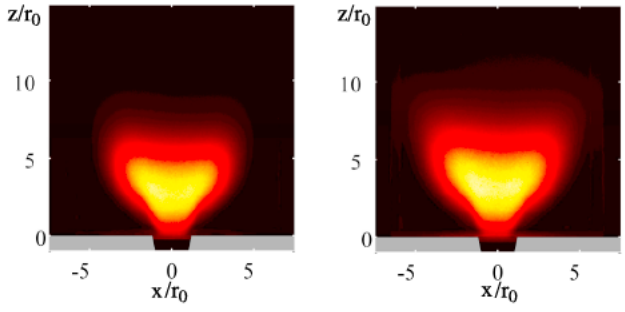

(a) Flame A : $CH_4/O_2/N_2$, X_{N_2} = 0.79, S_L = 37 cm/s, T_{ad} = 2200 K, U_b = 14.3 m/s.

(b) Flame B: $CH_4/O_2/CO_2$, X_{CO_2} = 0.68, S_L = 21 cm/s, T_{ad} = 2200 K, U_b = 9.7 m/s.

Fig. 1. OH* intensity distributions of the N_2- and CO_2-diluted CH_4/O_2 swirling flames at equivalence ratio ϕ = 0.95, swirl number S_0 = 0.75 and thermal power P = 13 kW. Grey elements indicate solid components of the combustor.

2. The experimental setup

2.1. OXYTEC test-rig

The setup is fully described in [8], only the main components are reported here. The combustion chamber has a square cross section of 150 mm width and 250 mm height equipped with four quartz windows as illustrated in Fig. 2. The combustion chamber ends with a converging nozzle with an area contraction ratio of 0.8. The burned gases are exhausted to the atmosphere at ambient pressure.

The swirler is an axial-plus-tangential entry swirl generator allowing to adjust the swirl level at the injector outlet by modifying the distributions of the mass flow rates injected tangentially $\dot{m}_\theta$ and axially $\dot{m}_z$. The swirl number is here set to S_0 = 0.75 for both flames investigated.

Methane is first mixed within the swirler with the oxidizer mixture O_2/N_2 or O_2/CO_2. Further details on the injection systems can be found in [16]. The flammable mixture leaves the swirler through a r_0 = 10 mm cylindrical channel and flows into the combustion chamber through an end piece of height $h = r_0$ equipped with a diffuser with a cup angle $\beta = 10°$.

The metallic combustion chamber back plane, which is in contact with the burned gases, is cooled by water circulation. The position of the cooling device is indicated in Fig. 2. The temperature close to the heat exchanger is measured with thermocouples inserted in the stainless steel surrounding the cooling circuit. After ignition, when the chamber has reached steady thermal conditions, the wall temperature is typically 81 °C at the inlet of the heat exchanger and 99 °C at its outlet, with no significant difference between operation with Flame A (N_2-diluted) and Flame B (CO_2-diluted).

Table 1 summarizes the operating conditions for the two selected flames. The adiabatic flame temperature T_{ad} and laminar burning velocity S_L are calculated with the GRI 3.0 mechanism and a dedicated 1D flow solver.

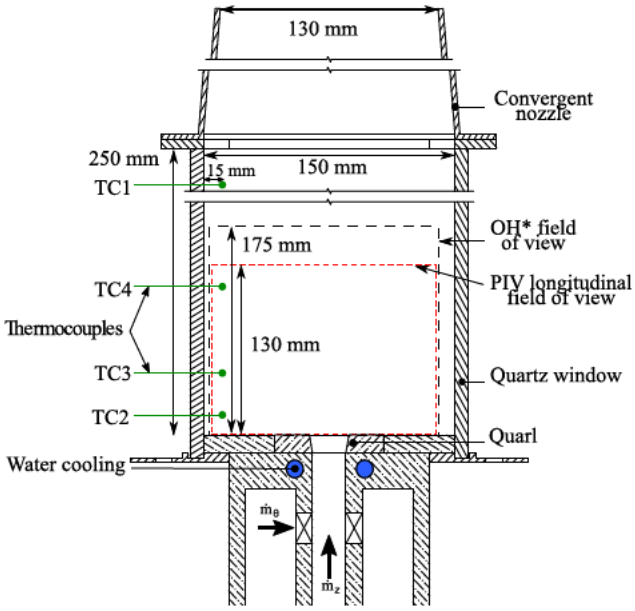

Fig. 2. OXYTEC atmospheric test-rig.

Table 1
Combustion parameters for the two selected flames. S_L : laminar burning velocity. U_b : bulk velocity in the injection tube. Re: Reynolds number based on the injection diameter D and U_b. X_d : diluent (N_2 or CO_2) molar fraction. T_{ad} : adiabatic flame temperature. S_0 : swirl number.

	ϕ	P [kW]	S_L [cm/s]	U_b [m/s]	Re	X_d	T_{ad} [K]	S_0
N_2-diluted Flame A	0.95	13	37	14.3	15900	0.79	2200	0.75
CO_2-diluted Flame B	0.95	13	21	9.7	13000	0.68	2200	0.75

2.2. Diagnostics

The flame topology is analyzed with OH* chemiluminescence images. The structure of the velocity field under reacting conditions is determined by Particle Image Velocimetry (PIV) measurements in an axial plane. The OH* and PIV data are taken from [8] where a full description of these diagnostics is given.

The temperature in the hot gases is measured with R-type thermocouples (10% Rh/Pt). Two thermocouples of bead diameter 200 μm and 450 μm are used to correct the measured temperature from radiative heat losses with the reduced radiation error method described in [17,18]. As sketched in Fig. (2), probes are introduced in the burned gases at the combustor outlet (TC1 at $z_1 = 205$ mm and TC4 at $z_4 = 110$ mm) and inside the outer recirculation zone of the swirling flow (TC2 at $z_2 = 15$ mm and TC3 at $z_3 = 40$ mm).

The development of Laser Induced Phosphorescence (LIP) [19] allows relatively convenient measurements of temperatures over large surfaces with a high precision and over a large dynamic range [20,10]. Surfaces of interest are coated with a thermographic phosphor. When excited in the ultraviolet, the visible luminescence signal provides an information on the surface temperature. This technique is here used to determine the surface temperatures of the internal metallic combustor back plane wall and the internal and external wall temperatures of the quartz windows of the combustion chamber to infer the wall heat flux distribution.

The LIP setup is represented in Fig. 3. A phosphorescent $Mg_{3.5}FGeO_5$:Mn powder (Phosphor-Technology, EQD25/N-U1) mixed with a high temperature binder (ZYP Coatings, HPC Binder) is coated on the surface of interest. Excited with a Nd:YAG laser quadrupled at 266 nm with a 3 Hz repetition rate (Continuum, Minilite ML II), the phosphor yields a luminescence signal with a peak emission centered at 660 nm. The temporal response of this signal is recorded with a photomultiplier with a rise time of 5 ns (Hamamatsu, R9880U-20). The electrical signal is amplified with a resistance and an operational amplifier with a rise time of 10 ns (HCA-40M-100K-C). The electrical signal is finally recorded with a 350 MHz oscilloscope (LeCroy WaveSurfer 434). The response of the phosphor to the laser impulse follows an exponential decay $I(t) = I_0\exp(-t/\tau)$, where the decay time τ is a function of the phosphor temperature. To obtain the decay time τ, each response curve is analyzed within a window between instants $t_1 = c_1\tau$ and $t_2 = c_2\tau$ with an iterative Matlab® routine, where c_1 and c_2 are two positive constants.

The LIP system is calibrated with the same acquisition setup and by recording the signal emitted by the tip of a heated thermocouple coated with the same phosphorescent paint. The decay time of the phosphorescent signal is measured and associated to the temperature recorded by the thermocouple following the procedure described in [21]. The resulting calibration curve is represented in Fig. 4, where the phosphor decay time is plotted for temperatures ranging from 300 K up to 1200 K with an electrical heater and a flame for the highest temperatures. A sensitivity analysis has been made by varying c_1 and c_2 in order to minimize the standard deviation of the signal at 300 K. The retained values $c_1 = 0.4$ and $c_2 = 6.0$ yield the best results with a weak scatter of the data in Fig. 4 limited to ± 9 K at 500 K, ± 2 K at 750 K, ± 7 at 1000 K and ± 15 K at 1100 K.

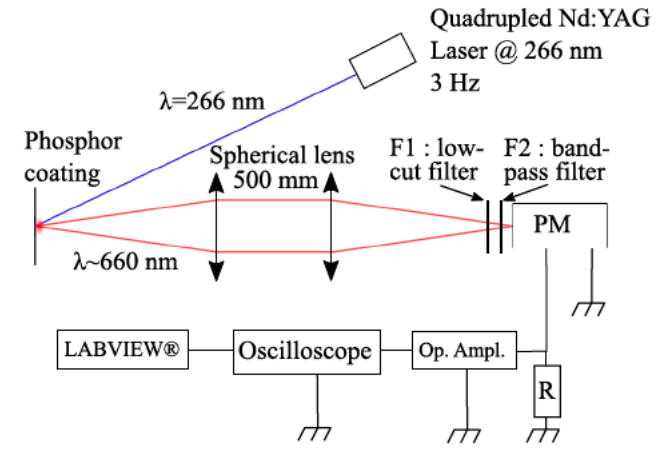

Fig. 3. Experimental setup and acquisition chain for Laser Induced Phosphorescence measurements.

3. Results and discussions

3.1. Wall temperature distributions

The LIP bench with the laser is set on a pivoting arm. This setup is used to determine the temperature of the internal metallic surfaces inside the combustion chamber. The temperature on the internal and external surfaces of the quartz windows are also measured along the axial direction and a set of transverse directions, as displayed in Fig. 5. The temperature along the exhaust nozzle external surface and along two perpendicular directions of the combustion chamber dump plane are also determined. This detailed thermal characterization is also motivated by the need to provide wall temperatures as boundary conditions for numerical reactive flow simulations.

The temperature profiles T_i(z) and T_e(z) at the internal and external

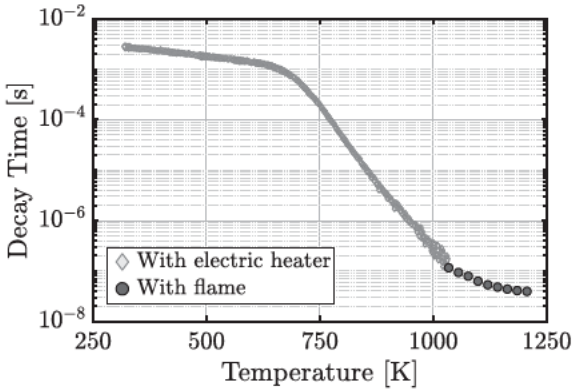

Fig. 4. Calibration curve for LIP plotting the phosphorescent signal decay time of the Mg-phosphor as a function of its temperature. Results were obtained with an electrical heater (losanges) and a flame (circles). Each of the 1100 losanges represents a laser shot and the circles represents the mean value averaged over 70 shots.

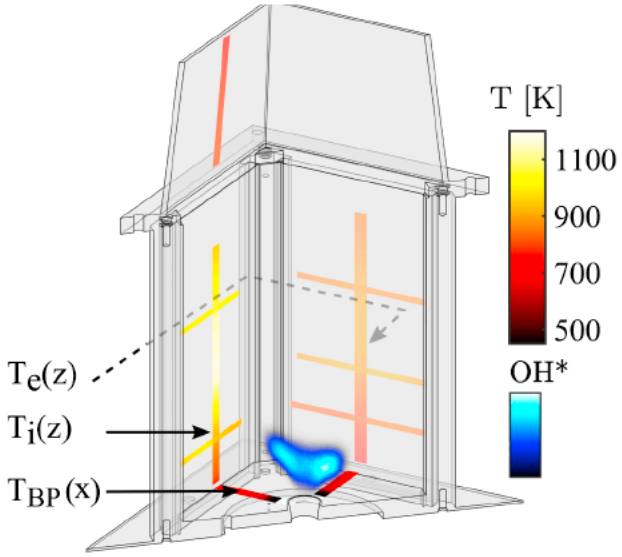

Fig. 5. Cut of the test rig with the temperature distributions measured by LIP for Flame A (N_2-diluted). The OH* chemiluminescence intensity is superimposed to appreciate the distribution of the combustion reaction within the combustion chamber volume with respect to the temperature profiles along the walls. Internal (T_i) and external (T_e) temperatures of the quartz windows. T_{BP}: temperature of the combustion chamber dump plate. Note that T_{BP} is measured on both sides of the injector, but is only represented here in a corner.

sides of a quartz window are shown in Fig. 6(a). These temperatures are determined all along the quartz window, except for the external surface with the CO_2-diluted flame B. At each height z, 25 samples of temperatures are recorded. The standard deviation of the signal is plotted with error bars in Fig. 6(a) at $z/r_0 = 3.0$, 8.0 and 12.5. Scattering of the data is small and hardly visible. At the highest temperature recorded, the standard deviation is around $T_{rms} \simeq 35$ K. The same measurements (not shown here) were repeated a month apart, and exhibited a very good reproducibility of less than 20 K.

Along the cooled combustion chamber dump plane, temperatures of the metallic part remain moderate at about 700 K (see $T_{BP}(x)$ in Fig. 5). The difference between the internal and external surface temperature of the quartz window $\Delta T = T_i(0) - T_e(0)$ remains small close to the combustion chamber back plate in Fig. 6(a), $\Delta T \simeq 100$ K. The temperature then progressively increases along the sidewalls further downstream until a plateau is reached at $z/r_0 \sim 8$ for Flame A and a bit further upstream $z/r_0 \sim 6$ for Flame B. The maximum temperature reached by the quartz window internal and external surfaces are then respectively $T_i^m = 1180$ K and $T_e^m = 942$ K for Flame A and $T_i^m = 1189$ K and $T_i^m = 961$ K for flame B. The difference $T_i^m - T_e^m \simeq 233$ K remains however the same in both cases. The temperature then smoothly drops further downstream when approaching the exhaust nozzle. The main differences in Fig. 6(a) are that the CO_2-diluted flame B yields slightly hotter wall temperatures than the N_2-diluted flame A at the bottom of the combustor, and cooler wall temperatures further downstream in the combustion zone.

The temperature profiles along the combustion chamber back plate shown in Fig. 6(b) feature no differences between the N_2- and the CO_2-diluted flames. The temperature is determined on both sides of the injector for the N_2-diluted flame to assess the flow symmetry (left and right profiles of dark symbols). The combustion chamber flange is a thick plate into which the diverging cup of the injection nozzle is screwed. The outer diameter of this cup is $3r_0$ and this component is directly in contact with the water cooling system. These features allow to interpret the temperature distributions shown in Fig. 6(b). At $x = \pm 7.5r_0$, the quartz/metal contact imposes a temperature of $T_{BP} = 700$ K, the temperature then slightly decreases down to $x = \pm 3r_0$, where a sudden drop of 300 K takes place. This location corresponds to

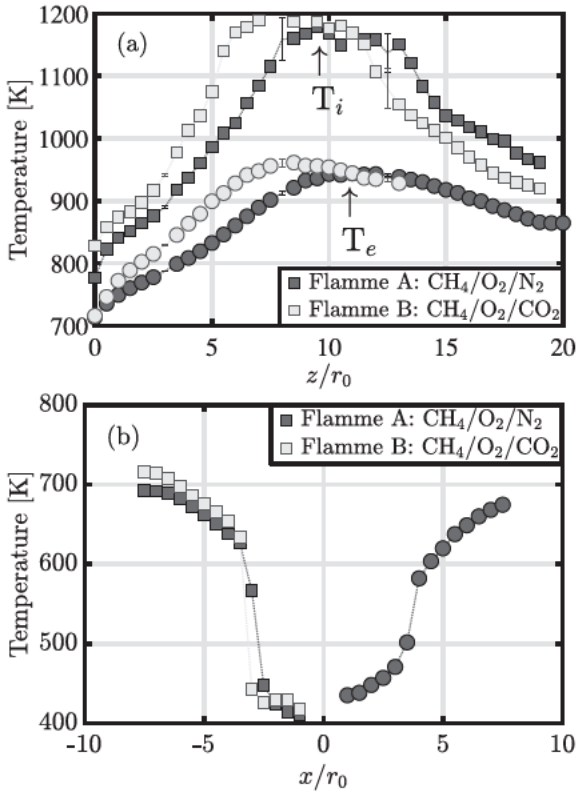

Fig. 6. Top: Temperature evolution along the internal $T_i(z)$ (squares) and external $T_e(z)$ (circles) surfaces of the quartz window as a function of the height z. Bottom: Temperature evolution along the combustor dump plane $T_{BP}(x)$ as a function of the transverse coordinate x. N_2-diluted flame A: dark symbols. CO_2-diluted flame B: bright symbols.

the metal/metal contact between the combustion chamber flange and the water cooled injector diffuser cup. Finally, the temperature profile close to the injector nozzle outlet remains flat with temperatures below 450 K.

The main conclusion is that the temperatures measured along the internal walls of the combustor are barely altered between the N_2- and the CO_2-diluted flames, except that they are shifted. It is now worth examining the corresponding conductive heat flux through the walls.

3.2. *Wall heat flux distributions*

For the CO_2-diluted flame ($X_{CO_2} = 0.68$) radiative heat transfer to the walls are significantly enhanced compared to air operation [22], and the first objective is to infer from LIP measurements the heat load on the sidewalls of the combustor. The second objective is to elucidate the reason for the close distributions of the wall temperatures measured for Flame A and Flame B, despite their very large differences in CO_2 concentrations in the burnt gases. A model for the heat transfer through the quartz windows, which constitute the largest surfaces in contact with the reactive flow is derived in the following.

Heat transfers are characterized by conductive heat flux φ^{cd} inside the quartz window and the metallic components, and by the convective φ^{cv} and radiative φ^{rad} heat fluxes within the flow. It is at this stage assumed that the quartz material is opaque to radiation for the wavelengths of interest, as will be later shown. Along the internal surface of the quartz window, the energy balance yields:

$$\varphi^{cv}(z) + \varphi^{rad}(z) = \varphi^{cd}(z) \tag{1}$$

In this case, the conductive heat flux through the quartz window φ^{cd} is also the total heat flux.

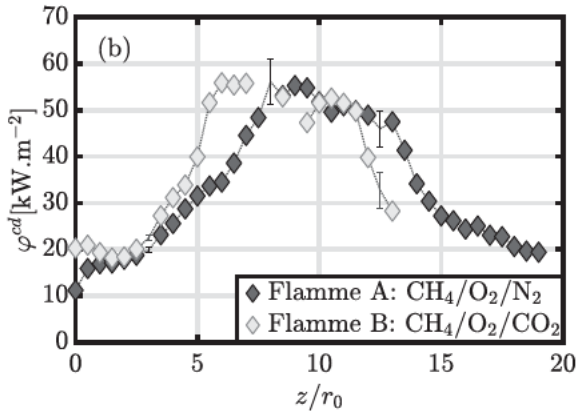

Fig. 7. Distribution of the conductive heat flux through the quartz window as a function of the height z. The standard deviation is indicated at $z/r_0 = 3.0$, 8.0 and 12.5.

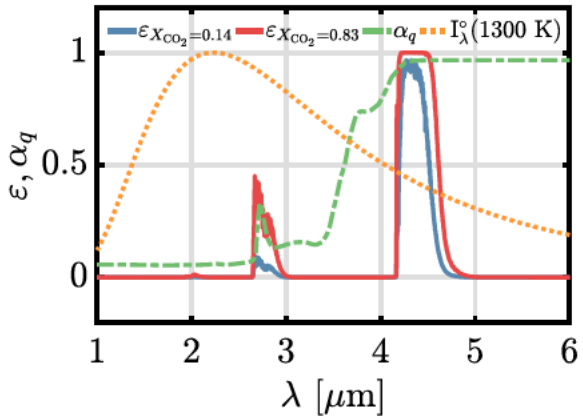

Fig. 8. Spectral characterization of the quartz window. Dashed green line: spectral absorbance of the quartz window computed for a thickness $e = 8$ mm. Solid line: CO_2 emissivity spectrum at 1300 K, $X_{CO_2} = 0.14$ as in the burned gases in flame A (blue), and $X_{CO_2} = 0.83$ as in flame B (red). Emissivity is calculated with line by line model, using HITEMP 2010 database [25], with a gas column of $l = 8$ cm and a resolution of 25 cm^{-1}. Dotted orange line: black-body radiation at 1300 K. (For interpretation of the references to colour in this figure legend, the reader is referred to the web version of this article.)

3.2.1. Conductive heat flux through the quartz window

The conductive heat flux $\varphi^{cd}(z)$ is derived from Fourier's law:

$$\varphi^{cd}(z) = \frac{1}{e}\int_{T_e(z)}^{T_i(z)} k(T)\mathrm{d}T \tag{2}$$

where e is the thickness of the quartz window and k is the thermal conductivity of the quartz material which depends on temperature. The thermal conductivity is approximated with the data from the manufacturer Heraeus [23] and the polynomial relation [24]:

$$\frac{k(T)}{k_0} = \beta_0 + \beta_1\left(\frac{T}{T_0}\right) + \beta_2\left(\frac{T}{T_0}\right)^2 + \beta_3\left(\frac{T}{T_0}\right)^3 \tag{3}$$

where $k_0 = 1.38$ W.m.K^{-1} is the thermal conductivity at $T_0 = 293$ K and the coefficients are $\beta_0 = 1.02$, $\beta_1 = -0.179$, $\beta_2 = 0.186$ and $\beta_3 = 0.0216$.

The conductive heat flux $\varphi^{cd}(z)$ is therefore calculated with the temperature profiles from Fig. 6(a). Each position being scanned with 25 samples of wall temperature, Eq. (2) is evaluated at each height z for every combination of the recorded samples for the internal T_i and the external T_e temperatures of the quartz windows. This yields the mean value and the standard deviation for $\varphi^{cd}(z)$. Results are shown in Fig. 7 for flames A and B. The standard deviation of the data remains lower than $\varphi^{cd}_{rms} < 5$ kW. m^{-2}. It appears that the heat flux is very close in both cases. Starting from $\varphi^{cd} \simeq 20$ kW.m^{-2} until $z = 4r_0$, the conductive heat flux increases up to 56 kW.m^{-2} at a height noted z_c. It then suddenly decreases to reach a plateau at 50 kW.m^{-2}, for the CO_2-diluted flame B at $z_c \simeq 5.5r_0$, and at $z_c = 8.0r_0$ for N_2-diluted flame A. Beyond $z \simeq 11r_0$, the conductive heat flux rapidly drops with the downstream distance to the combustor flange. Data are collected up to $z = 20r_0$ for the N_2-diluted flame. At this distance, the conductive heat flux drops to $\varphi^{cd} \simeq 20$ kW.m^{-2}. These data can be useful to validate numerical flow simulations including conjugate heat transfer to predict the wall temperature and wall heat flux fields.

One recalls that only small differences between the wall temperature distributions were found in the previous section for flame A and flame B. It is here highlighted that the conductive heat flux through the quartz windows inferred from the difference of the surface temperatures on both sides of the window is also very close for both flames. Enhancement of the burned gases emissivity for the CO_2-diluted flame B does not lead to increased heat losses through the windows. These two important features are analyzed in the subsequent section.

3.2.2. Radiative and convective heat fluxes

The radiative flux results from complex interactions between the burned gases themselves and between the burned gases and the solid boundaries of the combustor. The quartz window and the burned gases are two semi-transparent materials, whose spectral properties must now be detailed. This enables to check wether the similarity between the total heat flux plotted in Fig. 7 for flames A and B featuring very different burned gas compositions with different radiative properties cannot be explained by the quartz window transparency.

The radiative properties of flame A and B burned gases are mainly determined by their concentration of CO_2 and H_2O. Soot emission has not been observed in any of the two flames operating at fuel lean conditions and which appear blue by direct eye view. There is thus no need to consider this contribution to thermal radiation. Besides, as the water vapor molar fraction X_{H_2O} does not vary much between these two flames, its effects on the radiative heat transfer are therefore also disregarded in the following analysis.

The quartz window and the CO_2 spectral properties are represented in Fig. 8. The CO_2 emissivity is calculated using the Line-By-Line HITEMP 2010 database [25]. The molar fraction of CO_2 has been set to the same values $X_{CO_2} = 0.14$ and 0.83 as in the burned gases composition of the N_2- and CO_2- diluted flame. The column length has been set to 8 cm, which is the minimal distance between the quartz window and the injector. The emissivity spectrum is calculated with a 25 cm^{-1} resolution, and plotted at the wavelengths of interest determined by the radiation I^*_λ of a black-body at the characteristic temperature of the burned gases $T_{gas} \simeq 1300$ K. This temperature is lower than the adiabatic flame temperature due to heat losses. The absorbance of the quartz window made of fused silica is calculated from the transmittance curve provided by the manufacturer (Infrasil $^{\circledast}$ 301/ 302, [23]). The CO_2 main peak emissivity band is located around $\lambda = 4.3\,\mu$m, in the same spectral range as the absorption region of the quartz window. It results that the CO_2 emission is almost integrally absorbed by the quartz window at 4.3 μm. This analysis proves that the similar total heat flux found for flame A and B cannot be attributed to the quartz window transparency. A coarse estimation of both radiative and convective heat fluxes is therefore needed.

Fig. 8 also indicates that CO_2 can be considered as optically thick around 4.3 μm. This feature is here highlighted for the burned gases from both the N_2- and CO_2-diluted flame, in which the value for the CO_2 main peak emissivity band is closed to unity. The first effect of this optically thick medium is to enhance CO_2 re-absorption within the burned gases leading to an homogenization of the temperature of these gases [13,15]. The second effect is that the internal surface of the quartz window mainly absorbs the radiation from the burned gases located in its vicinity. Assuming an equivalent gas column of length L emitting to

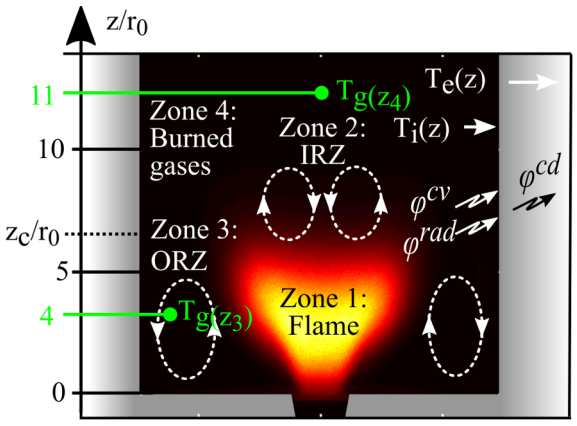

Fig. 9. Separation of the combustion chamber volume in different zones to model the heat transfer to the sidewalls.

the surrounding walls, the radiative flux is expressed as [26,27]:

$$\varphi^{rad} \sim \sigma(\varepsilon(L)T_g^4 - \beta_g T_i^4) \tag{4}$$

where T_i is the temperature of the internal surface of the quartz window, $\varepsilon(L)$ and T_g are the equivalent emissivity and the temperature of the burned gases and β_g the gas absorptivity. The absorptivity β_g is correlated to $\varepsilon(L)$ as $\beta_g/\varepsilon(L) = (T_g/T_i)^{1.5}$ [26] and this correlation is injected in Eq. (4) yielding:

$$\varphi^{rad} \sim \varepsilon(L)\sigma T_g^{1.5}(T_g^{2.5} - T_i^{2.5}) \tag{5}$$

Modest [28] gives a rough approximation of the mean beam length $L = 3.6V/A$ that gives satisfying results, where V and A are the volume and the surrounding surface area of the considered region.

Along the combustor walls, the swirling flow is turbulent. The Ditus correlation [29] is used to estimate the convective heat flux:

$$\begin{cases} \varphi^{cv} = h^{cv}(T_g - T_i) \\ \mathrm{Nu}_L = \frac{h^{cv}L}{k_a} = 0.023\mathrm{Pr}^{1/3}\mathrm{Re}_D^{4/5} \end{cases} \tag{6}$$

where k_a is the thermal conductivity of the burned gases at $T_b = (T_g + T_i)/2$, L the height of the combustion chamber, Nu_L, Pr are the Nusselt and Prandtl numbers and Re_D is the Reynolds numbers based on the hydraulic diameter D of the square cross section area of the combustion chamber and is also evaluated at T_b.

3.3. Analysis of heat transfer regimes

In order to discriminate the origin of the thermal loads on the sidewalls, the combustion chamber volume is separated into four distinct zones, as sketched in Fig. 9:

1. — Zone 1 corresponds to the reaction region, where the temperature is close to the adiabatic flame temperature T_{ad} and the axial velocities are high at the injector outlet. This zone corresponds to the volume delimited by the spontaneous OH^* emission shown in Fig. 1a and b and lies far from the walls.
2. Zone 2 corresponds to the Inner Recirculation Zone (IRZ) of the swirling flow and is revealed by the axial velocity field plotted in Fig. 10. Recirculation of the burned gases inside the IRZ allows flame stabilization in the center of the combustor, but this region is not in direct contact with the combustor sidewalls.
3. Zone 3 corresponds to the Outer Recirculation Zone (ORZ) highlighted in the bottom corners in Fig. 10, which is located between the flame front, the combustor sidewalls and the combustor flange. This region is essentially filled with burned gases and characterized by large-scale vortical structures and low velocities. The temperature in this region is measured with a thermocouple, represented in Fig. 9 at $z_3 = 4r_0$ (TC3 in Fig. 2). The small flow velocities in this region indicate that the convective heat transfer coefficient h^{cv} at the quartz windows remains small in this zone. Wall radiative energy transfers are presumed to be more important in this region. The ORZ stops at the height $z_c \simeq 8r_0$.
4. The last region designated as zone 4 in Fig. 9 corresponds to the burned gases near the combustion chamber exhaust. The temperature is also relatively homogeneous in this region and was measured with a thermocouple at $z_4 = 11r_0$ (TC4 in Fig. 2). The flow pattern induced by the swirling motion forces the burned gases to circumvent the large IRZ and to be redirected toward the walls with relatively large velocities (see Fig. 10). This flow circulation promotes wall convective heat transfer.

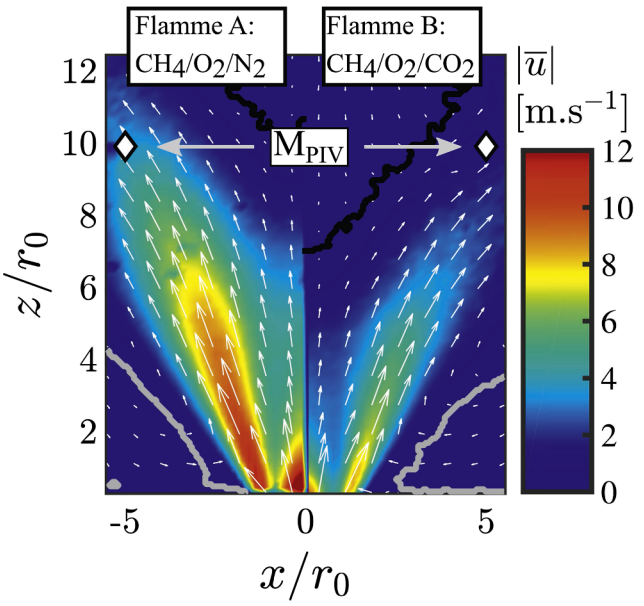

Fig. 10. 2D velocity fields in an axial plane in reacting conditions. $\phi = 0.95$, $P = 13$ kW, $S_0 = 0.75$ and $T_{ad} = 2200$ K. The IRZ and ORZ are delineated by the black and grey thick contours and correspond to $u_z = 0$.

In this analysis, it is hypothesized that the two important zones for heat transfer to the quartz walls are zones 3 and 4. Radiative effects from zone 1 and zone 2 are discarded due to an optically thick approximation of radiative energy transfer. In zone 3, only radiative heat transfer is then considered due to the low velocities of the flow in this region. In zone 4, both the radiative and convective heat fluxes are taken into account. Table 2 synthesizes the different temperatures, radiative and thermal properties that are used to make the calculations with the model presented in Section 3.2. The thermal load on the combustor sidewalls is now analyzed with Eqs. (5) and (6) and results are compared for flame A and flame B. Simplifications are made based on the similarities of the flame (Fig. 1) and flow (Fig. 10) patterns.

The gas temperatures T_g measured with a thermocouple at $z_3 = 4r_0$ and $z_4 = 11r_0$ are chosen to fix the temperature throughout zone 3 (ORZ) and zone 4 (Burned gases). The mean beam length method from Modest [28] is used to determine the radiative properties of the major species within the burned gases. Data from Riviere and Soufiani [30] are used to calculate the total emissivity $\varepsilon(L)$ of the burned gases while accounting for both CO_2 and H_2O molar fractions. The value found for the CO_2-diluted flame B is twice the emissivity of the N_2-diluted flame A: $\varepsilon_B(L) \simeq 2\varepsilon_A(L)$.

In the ORZ corresponding to zone 3, the temperature difference $\Delta T = T_g - T_i$ between the burned gases temperature T_g, measured with a thermocouple, and the internal surface temperature T_i of the quartz

Table 2
Heat transfer budget in zones 3 and 4 for the N_2- (Flamme A) and CO_2- (Flamme B) diluted flames.

Flame	Dil.	$X_{CO_2}^{burned}$	$\varepsilon(L)$	Zone 3 (ORZ): $z_3 = 4r_0$			Zone 4 (BG): $z_4 = 11r_0$				
				$T_g(z_3)$ [K]	$T_i(z_3)$ [K]	Eq. (5) [kW.m^{-2}]	$T_g(z_4)$ [K]	$T_i(z_4)$ [K]	$U_z(z_4)$ [m/s]	Eq. (5) [kW.m^{-2}]	Nu^L
A	N_2	0.14	0.042	1355	937	4.8	1393	1168	4	3.2	25
B	CO_2	0.83	0.081	1260	1013	4.9	1364	1169	1.4	5.1	18

window, measured with LIP, at the height $z_3/r_0 = 4$ is roughly twice larger for the N_2-diluted flame A ($\Delta T = 418$ K), than for the CO_2-diluted flame B ($\Delta T = 247$ K).

As displayed in Table 2, the radiative flux estimated with Eq. (5) leads to close values between flame A and flame B. Thus, the redistribution observed for the flow temperature in the ORZ (zone 3 in Fig. 9) and at the bottom of the quartz window between flame A and B implies that the radiative flux φ_3^{rad} barely differs in this region between the two configurations. As in the ORZ, the convective heat transfer remains small compared to the radiative contribution $\varphi_3^{cv} \ll \varphi_3^{rad}$, the conductive heat flux through the quartz window $\varphi_3^{cd} \simeq \varphi_3^{rad}$ is the same for flame A and B in zone 3. This conclusion corroborates the total heat fluxes determined from LIP measurements made in Fig. 7 for $z/r_0 < 5$.

A different heat transfer process takes place in zone 4. In this region, the difference between the internal quartz wall temperature T_i and the burned gases temperature T_g measured at $z_4 = 11r_0$ is close for flame A ($\Delta T_{N_2} = 225$ K) and flame B ($\Delta T_{CO_2} = 195$ K). In this case, the radiative flux φ_4^{rad} for the CO_2-diluted flame B takes a much higher value than for the N_2-diluted flame A in zone 4. To fully interpret the origin of convective heat transfer in this zone, one needs to examine the velocity fields measured by PIV, which are represented in Fig. 10. The two flames exhibit the same flow pattern, but the velocities are much higher for the N_2-diluted flame A. Since the PIV field of view does not reach the combustor sidewalls in Fig. 10, the point M_{PIV} located at the height $z = 10r_0$ and $x = 5r_0$ is selected to compare the velocities reached by the flow in zone 4 between flame A and flame B. It appears that at this point $u_z \simeq 4.0$ m.s^{-1} for flame A and $u_z \simeq 1.4$ m.s^{-1} for flame B. The convective heat transfer coefficient h_4^{cv} between zone 4 and the window therefore takes a higher value for flame A than for flame B. The main reason for this velocity difference between flame A and B is that the combustion parameters of the CO_2-diluted flame B are selected to match the same adiabatic flame temperature T_{ad} and the same thermal power P as the N_2-diluted flame A. In this case, the volume flowrate injected in the system is much smaller for flame B compared to flame A due to the higher molecular weight of carbon dioxide compared to nitrogen. The Nusselt number based on the velocities measured at the point M_{PIV} for both flame A and B is shown in Table 2 and is higher for the N_2-diluted flame. One may then attempt the qualitative following interpretation: the higher radiative flux φ_4^{rad} of flame B in zone 4 is partly compensated by a higher convective heat flux φ_4^{cv} for flame A in the same zone leading to about the same conductive heat flux φ^{cd} through the quartz window for both flames in zone 4.

4. Conclusion

The surface temperatures along the combustor walls have been determined with Laser Induced Phosphorescence measurements for two flames featuring the same thermal power, equivalence ratio and adiabatic flame temperature, but a different diluent. Though, for the investigated combustor, switching from aero-combustion to CO_2-diluted oxy-combustion does not alter much the wall temperatures and the heat flux through the sidewalls of the combustion chamber, the experiments and analysis made in this study show that it has disrupted the origin of heat transfer in two different manners.

A model coupled to gas and wall temperature measurements has been used to estimate the heat transfer mechanisms prevailing in the outer recirculation region of the swirling flow filled with burned gases and in the burned gases exhausting the combustion chamber. At the bottom of the combustion chamber, in the outer recirculation region of the flow, it has been shown that the radiative wall heat flux takes similar values between the two flames investigated because the higher difference of temperature between the hot gases and the internal surface of the quartz window for the N_2-diluted flame counterbalances the higher radiative emission from the gases produced by the CO_2-diluted flame. Downstream the reaction zone, the radiative flux to the wall in the upper region of the combustor is more important for the CO_2-diluted flame, whereas the convective heat transfer is more important for the N_2-diluted flame. These conclusions have been used to interpret the comparable levels and distributions measured for the total heat flux lost through the quartz walls between the two flames.

Therefore, while the additional contribution of the radiative flux due to the large CO_2 concentration in oxy-burners operating with dry flue gas recirculation would a priori lead to enhance the thermal load to the combustor walls, a complex re-balancing of the heat flux has been instead emphasized in this study. This thermal redistribution underlines the coupling between the flow pattern and the radiative effects of the burned gases as already observed in [15] for air-powered systems.

While rough approximations have been admittedly made to develop a low order model allowing to qualitatively interpret the observed features, more sophisticated tools are needed to better characterize the influence of CO_2 dilution on the conductive and radiative heat wall fluxes inside the combustor.

Acknowledgments

This work is supported by the Air Liquide, Ecole CentraleSupélec and CNRS Chair on oxy-combustion and heat transfer for energy and environment and by the OXYTEC project (ANR-12-CHIN-0001) from Agence Nationale de la Recherche. We also would like to thank the technical staff of EM2C for their assistance during the design and construction of the experimental setup.

References

[1] Buhre B, Elliott L, Sheng C, Gupta R, Wall T. Oxy-fuel combustion technology for coal-fired power generation. Prog Energy Combust Sci 2005;31:283–307. https://doi.org/10.1016/j.pecs.2005.07.001.
[2] Anderson RE, MacAdam S, Viteri F, Davies DO, Downs JP, Paliszewski A. Adapting gas turbines to zero emission oxy-fuel power plants. ASME Paper GT2008-51377. 2008.
[3] Cieutat D, Sanchez-Molinero I, Tsiava R, Recourt P, Aimard N, Prébendé C. The oxy-combustion burner development for the CO2 pilot at lacq. Energy Procedia 2009;1:519–26. https://doi.org/10.1016/j.egypro.2009.01.069. http://www.sciencedirect.com/science/article/pii/S1876610209000708.
[4] Perrin N, Paufique C, Leclerc M. Latest performances and improvement perspective of oxycombustion for carbon capture on coal power plants. Energy Procedia 2014;63:524–31. https://doi.org/10.1016/j.egypro.2014.11.057. http://www.sciencedirect.com/science/article/pii/S1876610214018724.
[5] Amato A, Hudak B, D'Carlo P, Noble D, Scarborough D, Seitzman J, Lieuwen T. Methane oxy-combustion for low CO2 cycles: blowoff measurements and analysis. J Eng Gas Turbines Power 2011;133:061503. https://doi.org/10.1115/1.4002296.
[6] Watanabe H, Shanbhogue S, Taamallah S, Chakroun N, Ghoniem A. The structure of swirl-stabilized turbulent premixed CH_4/air and $CH_4/O_2/CO_2$ flames and

mechanisms of intense burning of oxy-flames. Combust Flame 2016;174:111–9.
[7] Taamallah S, Chakroun N, Watanabe H, Shanbhogue S, Ghoniem A. On the characteristic flow and flame times for scaling oxy and air flame stabilization modes in premixed swirl combustion. Proc Combust Inst 2017;36:3799–807.
[8] Jourdaine P, Mirat C, Caudal J, Lo A, Schuller T. A comparison between the stabilization of premixed swirling co2-diluted methane oxy-flames and methane/air flames. Fuel 2017;201:156–64.
[9] Schmitt P, Poinsot T, Schuermans B, Geigle KP. Large-eddy simulation and experimental study of heat transfer, nitric oxide emissions and combustion instability in a swirled turbulent high-pressure burner. J Fluid Mech 2007;570:17–46.
[10] Guiberti TF, Durox D, Scouflaire P, Schuller T. Impact of heat loss and hydrogen enrichment on the shape of confined swirling flames. Proc Combust Inst 2015;35(2):1385–92.
[11] Tay-Wo-Chong L, Zellhuber M, Komarek T, Im HG, Polifke W. Combined influence of strain and heat loss on turbulent premixed flame stabilization. Flow Turbul Combust 2016;97(1):263–94.
[12] Gupta A, Modest MF, Haworth DC. Large-eddy simulation of turbulence-radiation interactions in a turbulent planar channel flow. J Heat Transfer 2009;131(6):061704.
[13] Zhang Y, Vicquelin R, Gicquel O, Taine J. Physical study of radiation effects on the boundary layer structure in a turbulent channel flow. Int J Heat Mass Transf 2013;61:654–66.
[14] Silvestri S, Patel A, Roekaerts D, Pecnik R. Turbulence radiation interaction in channel flow with various optical depths. J Fluid Mech 2018;834:359–84.
[15] Koren C, Vicquelin R, Gicquel O. Multiphysics simulation combining large-eddy simulation, wall heat conduction and radiative energy transfer to predict wall temperature induced by a confined premixed swirling flame. Flow Turbul Combust 2018:1–26.
[16] Jourdaine P, Mirat C, Caudal J, Schuller T. Stabilization mechanisms of swirling premixed flames with an axial-plus-tangential swirler. J Eng Gas Turb Power 2018;140:08152.
[17] Brohez S, Delvosalle C, Marlair G. A two-thermocouples probe for radiation corrections of measured temperatures in compartment fires. Fire Saf J 2004;39(5):399–411.
[18] Lemaire R, Menanteau S. Assessment of radiation correction methods for bare bead thermocouples in a combustion environment. Int J Therm Sci 2017;122:186–200.
[19] Brübach J, Pflitsch C, Dreizler A, Atakan B. On surface temperature measurements with thermographic phosphors: a review. Prog Energy Combust Sci 2013;39(1):37–60.
[20] Euler M, Zhou R, H.S., Dreizler A. Temperature measurements of the bluff body surface of a swirl burner using phosphor thermometry. Combust Flame 2014;161:2842–8.
[21] Guiberti T. Analysis of the topology of premixed swirl-stabilized confined flames [Ph.D. thesis]. Ecole Centrale Paris; 2015.
[22] Glarborg P, Bentzen LLB. Chemical effects of a high CO2 concentration in oxy-fuel combustion of methane. Energy Fuels 2008;22:291–6. https://doi.org/10.1021/ef7005854. arXiv: 10.1021/ef7005854.
[23] Heraeus, Quartz glass for optics data and properties quartz glass for optics data and properties (2013) 8.http://heraeus-quarzglas.com/media/webmedialocal/downloads/broschrenmo/DataandPropertiesOpticsfusedsilica.pdf.
[24] Combis P, Cormont P, Gallais L, Hebert D, Robin L, Rullier J-L. Evaluation of the fused silica thermal conductivity by comparing infrared thermometry measurements with two-dimensional simulations. Appl Phys Lett 2012;101(21):211908.
[25] Rothman L, Gordon I, Barber R, Dothe H, Gamache R, Goldman A, et al. Hitemp, the high-temperature molecular spectroscopic database. J Quant Spectrosc Radiat Transfer 2010;111(15):2139–50.
[26] Lefebvre AH, Herbert M. Heat-transfer processes in gas-turbine combustion chambers. Proc Inst Mech Eng 1960;174(1):463–78.
[27] Lefebvre AH, Ballal DR. Gas turbine combustion: alternative fuels and emissions. CRC Press; 2010.
[28] Modest MF. Radiative heat transfer. Academic press; 2013.
[29] Dittus F, Boelter L. Heat transfer in automobile radiators of the tubular type. Int Commun Heat Mass Transfer 1985;12(1):3–22.
[30] Rivière P, Soufiani A. Updated band model parameters for H_2O, CO_2, CH_4 and CO radiation at high temperature. Int J Heat Mass Transf 2012;55(13):3349–58.